communications earth & environment

Article

A Nature Portfolio journal

https://doi.org/10.1038/s43247-026-03466-3

Physical vertical fluxes decouple iron and manganese supply in the Southern Ocean

Thapelo Ramalepe[1,2] ✉, Alakendra N. Roychoudhury[2], Corentin Baudet[3], Andrew Bowie[4,5], Eva Bucciarelli[3], Natasha van Horsten[1,2,3,9], Pauline Latour[4,5,6], Hélène Planquette[3], Geraldine Sarthou[3], Yoshiki Sohrin[7], Linjie Zheng[7] & Thomas J. Ryan-Keogh[8]

Sub-nanomolar concentrations of dissolved iron and manganese seasonally limit phytoplankton growth in the Southern Ocean, as both are essential cofactors for metabolic processes. These trace metals are supplied from the subsurface to the surface through physical processes, including winter entrainment, diapycnal diffusion and Ekman pumping, where they are made available for biological uptake. Whilst the quantification of these processes for iron has been previously reported, no large-scale quantification exists for manganese in the Southern Ocean. We analysed regridded dissolved iron and manganese data from all available Southern Ocean cruises, to quantify these physical supply processes. Here we show that winter entrainment (18.58 ± 4.82 μmol m^{-2} yr^{-1} manganese; 29.78 ± 5.23 μmol m^{-2} yr^{-1} iron), followed by diapycnal diffusion (1.59 ± 1.51 μmol m^{-2} yr^{-1} manganese; 0.55 ± 1.58 μmol m^{-2} yr^{-1} iron), dominates the supply across the Southern Ocean. Matched low iron: manganese supply ratios along the zero meridian and near the Antarctic Peninsula suggest potential iron–manganese co-limitation, with the latter consistent with field observations in the Drake Passage. Accurately reproducing this spatial variability in models will improve projections of trace metal control on the Southern Ocean carbon pump.

The trace metals iron (Fe) and manganese (Mn) are essential micronutrients for phytoplankton growth and primary production in the Southern Ocean[1–3]. Despite being the 4th and 12th most abundant elements in the Earth's crust, respectively, both metals are largely depleted in the Southern Ocean surface waters[4,5], which can lead to regional phytoplankton growth limitation[6,7]. Southern Ocean phytoplankton have adapted to low Fe conditions through Fe-saving mechanisms, such as substitution of Fe-containing molecules (i.e., ferredoxin) and a decrease in the Fe-rich photosynthetic photosystems with a commensurate increase in photosynthetic antennae size[8,9]. Fe limitation can, to some extent, be compensated by Mn substitution in certain enzymatic systems involved in photosynthetic and antioxidant processes, allowing phytoplankton to maintain essential metabolic functions[10]. For example, diatoms produce more reactive oxygen species under Fe limitation and can substitute Mn to activate the antioxidant enzyme superoxide dismutase[11–13]. However, due to the depletion of both elements in Southern Ocean surface waters, this can lead to biochemical co-limitation, with both elements simultaneously limiting phytoplankton growth[6]. Furthermore, co-limitation occurs when phytoplankton's demand for these elements, both for growth and superoxide dismutase mechanisms, exceeds their availability[14]. Mn limitation can also be further intensified by competitive inhibition from zinc, which interferes with Mn uptake by phytoplankton; due to its higher concentration and stronger affinity for metal transporters[15,16]. Consequently, Fe–Mn colimitation in the Southern Ocean reduces phytoplankton productivity, which can influence carbon cycling in surface waters[6,17].

Both dissolved Mn and Fe (dMn and dFe; <0.2 μm) are redox-reactive elements whose bioavailability to phytoplankton is influenced by oxygen and light, with higher light promoting photoreduction of Mn and Fe oxides in surface waters[18,19]. In such conditions, their reduced forms are oxidized into insoluble forms, thereby reducing their availability to phytoplankton[19,20]. The Southern Ocean is characterized by sub-nanomolar concentrations of both metals, primarily due to its remoteness from land

[1]Southern Ocean Carbon-Climate Observatory, CSIR, Cape Town, South Africa. [2]Centre for Trace Metal and Experimental Biogeochemistry (TracEx), Department of Earth Sciences, Stellenbosch University, Stellenbosch, South Africa. [3]LEMAR, CNRS, IRD, Ifremer, IUEM, University Brest, Plouzané, France. [4]Institute for Marine and Antarctic Studies, University of Tasmania, Hobart, TAS, Australia. [5]Australian Antarctic Program Partnership (AAPP), University of Tasmania, Hobart, TAS, Australia. [6]ARC Australian Centre for Excellence in Antarctic Sciences (ACEAS), University of Tasmania, Hobart, TAS, Australia. [7]Institute for Chemical Research, Kyoto University, Uji, Japan. [8]National Oceanography Centre, Southampton, UK. [9]Present address: Department of Physics and Earth Sciences, Constructor University, Bremen, Germany. ✉e-mail: 22632816@sun.ac.za

and limited atmospheric inputs[21]. However, Mn and Fe concentrations can be locally increased by other external inputs like hydrothermal[22], sedimentary[23], and sea-ice melt sources[24]. Differences in their internal cycling and removal processes result in distinct water column distributions[25]. The distribution of trace metals at depth reflects large-scale mixing between distinct deep water masses, such as North Atlantic deep water (NADW) and Antarctic bottom water (AABW), which carry characteristic background concentrations at formation (e.g., deep NADW in the West Atlantic contains dFe in the range of approximately 0.3–0.7 nmol kg^{-1} and dMn in the South Atlantic around 0.10–0.16 nmol kg^{-1}, while AABW in the South Atlantic has dFe between roughly 0.3–0.5 nmol kg^{-1} and dMn near 0.16 nmol kg^{-1})[26,27], although Mn is rapidly removed during southward transport in NADW[25]. dMn profiles in the Southern Ocean typically show a scavenged-type profile, with low surface (<50 m) concentrations due to biological uptake and rapid removal, followed by a shallow subsurface maximum near ~100 m[21,25]. This subsurface increase is driven by remineralization and dissolution of the particulate Mn pool (pMn; >0.2 μm), mainly from labile and semi-labile fractions[28]. Below this depth, dMn concentrations decrease rapidly due to efficient scavenging. In contrast, dFe profiles often show a bioactive-type profile, with surface depletion caused by biological uptake and a more gradual increase with depth due to remineralization[29]. Dissolved Fe persists to deeper depths than Mn because it is strongly complexed by organic ligands, which reduce scavenging and stabilize Fe in the dissolved phase, together with additional deep-ocean sources, such as hydrothermal inputs[30]. The scavenging of Fe is primarily influenced by the concentration of dFe and the presence of iron complexing organic ligands, which stabilize Fe in the water column and prevent its rapid removal. When dFe concentrations exceed those of the ligands, scavenging rates increase, leading to a faster removal of dFe from the ocean interior than under ligand-saturated (ligand-excess) condition[31]. Some studies suggest that the same ligands that bind Fe^{3+} can also bind Mn^{3+}, decreasing its conversion to Mn^{2+}[32]. Removal of dMn is largely driven by the oxidation to pMn, where its oxidized form can scavenge itself and other trace metals, including Fe, from the ocean interior[32]. For Mn to be removed, its oxidation rate must exceed the reduction rate by bacteria, which converts it back to dMn[19].

In the Southern Ocean, remineralization of particulate species is the primary driver of internal dFe supply, particularly in regions where external inputs are limited[33]. This process replenishes the subsurface dissolved trace metal reservoirs[34]. While winter entrainment is recognized regionally as the main pathway delivering remineralized Fe, as well as hydrothermal and sedimentary sources, into the surface mixed layer[35,36], the relative contribution of these sources to both Fe and Mn across different Southern Ocean regions and their seasonal variability remain poorly quantified. During winter entrainment, deep vertical mixing driven by winds and air-sea buoyancy fluxes resets the mixed layer depth (MLD), entrains Mn and Fe into the surface ocean, and replenishes the dMn and dFe stocks[35,36]. Diapycnal diffusion[37], the vertical diffusion across density layers, Ekman pumping[38], wind-induced surface divergence and other physical processes, such as seasonal wind, lateral advection and storm-driven entrainment[39], all help to sustain this surface reservoir throughout the year.

During spring and summer, photoreduction of particulate trace metals can further supplement the dFe and dMn reservoir[40,41]. Whereas springtime detrainment—the subduction of surface waters out of the mixed layer—along with phytoplankton uptake and Ekman downwelling, acts as a sink, reducing mixed layer stocks. Particulate scavenging, another sink, shapes the vertical profile of dissolved trace metals by influencing their concentration gradient with depth. This gradient is crucial for estimating the vertical input of trace metals across the mixed layer. The depth at which the concentration gradient is greatest (i.e., nutricline), known as the manganocline for Mn (ZMn) and the ferricline for Fe (ZFe), helps identify where vertical physical processes are most dominant for trace metals[35,42]. In some cases, multiple depths may exhibit similarly strong gradients, especially in regions with layered water masses or active subsurface remineralization. In such cases, the shallowest depth is typically chosen as ZMn or ZFe, as it best represents a more relevant depth for vertical trace metal supply into the mixed layer[35]. Assessing the offset between the dMn and dFe gradients at the base of the maximum MLD (MLDmax) and the nutricline can provide insight into particulate scavenging depths and rates, remineralization processes, and contributions from deep-water sources, such that the nutricline can be deeper than the MLD[43,44].

While previous studies have demonstrated the importance of winter entrainment and diapycnal diffusion for Fe supply across the entire Southern Ocean[35,45], there is only one regional study for Mn in the Atlantic sector of the Southern Ocean[36]. Given the potential for Mn–Fe co-limitation in the Southern Ocean[6], it is essential to constrain this relationship with the physical supply pathways of both trace metals. This knowledge is important for understanding how primary production in this climate-regulating region may respond to shifts in trace metal concentrations[46], as the physical drivers of their fluxes are directly influenced by climate variability. Here we use the most recent trace metal data available from the GEOTRACES Intermediate Data Product (IDP) 2025[47] database for all open ocean Southern Ocean cruises (south of 30°S) and other data from GEOTRACES cruises (see "Methods") to quantify winter entrainment, Ekman pumping, diapycnal diffusion and detrainment, thereby determining the dominant physical processes driving dMn and dFe fluxes in this region. We further assess their extent by examining the offset between the maximum nutricline depth and MLDmax. When MLDmax approaches or exceeds the nutricline, winter mixing can entrain Fe- and Mn-rich waters into the mixed layer. Conversely, if MLDmax remains shallower than the nutricline, the physical supply of these metals is limited. This offset, therefore, reflects how changes in winds and buoyancy impact the delivery of Fe and Mn into the mixed layer. Furthermore, by computing the Fe and Mn colimitation tracer, Mn*, defined as the deficiency of dMn relative to dFe for phytoplankton growth, and directly comparing it to the ratio of total dFe supply to total dMn supply, we identify regions where the system is potentially co-limited by these elements.

Results and discussion

Nutricline depths shape the supply of Fe and Mn

Across the Southern Ocean, winter MLDmax ranged from 45 to 232 m, with the deepest mixed layers generally found south of the polar front (Supplementary Table 1). The depths of ZMn and ZFe ranged from 92–217 to 169–279 m, respectively, both tending to increase south of the polar front. Interbasin variation in ZMn was evident, with depths spanning 80–260 and 99–212 m in different regions, whereas ZFe showed relatively similar depth ranges (162–288 m) across the Southern Ocean. The ZFe observed here agrees with previous reports in the Southern Ocean, ranging between 100 and 300 m[35,42], most of which extend below the MLDmax[48]. In the Indian basin, ZFe was deeper than ZMn, indicating that a larger fraction of the Fe inventory is concentrated at deeper depths in the water column compared to Mn. As a result, Fe entrainment into surface waters requires deeper vertical mixing, driven by stronger winds, reduced stratification, or higher-magnitude buoyancy fluxes. Conversely, in the Atlantic and Pacific basins, the ZMn occurs deeper in the water column, where dMn concentrations are already decreasing with depth. As a result, entrainment of Mn into the surface mixed layer requires stronger physical fluxes compared with Fe, for which concentrations typically increase with depth. The resulting mean offset, the difference between the nutriclines and MLDmax, was 126 m for dMn (Fig. 1d) and 197 m for dFe (Fig. 1e), suggesting limited input of these trace metals into the mixed layer via different subsurface physical supply processes.

The supply of dMn and dFe to surface waters via diapycnal diffusion and Ekman pumping is controlled by both the magnitude of the vertical concentration gradients ($\partial dMn/\partial z$ and $\partial dFe/\partial z$) near the MLD, relative to the gradients at ZMn and ZFe. Mean $\partial dMn/\partial z$ at ZMn and $\partial dFe/\partial z$ at ZFe were both deeper than those at MLDmax in all basins of the Southern Ocean (Supplementary Fig. 1), indicating that diapycnal diffusion and Ekman pumping are most intense below the mixed layer and may not directly transport dFe and dMn vertically to the surface. The potential density

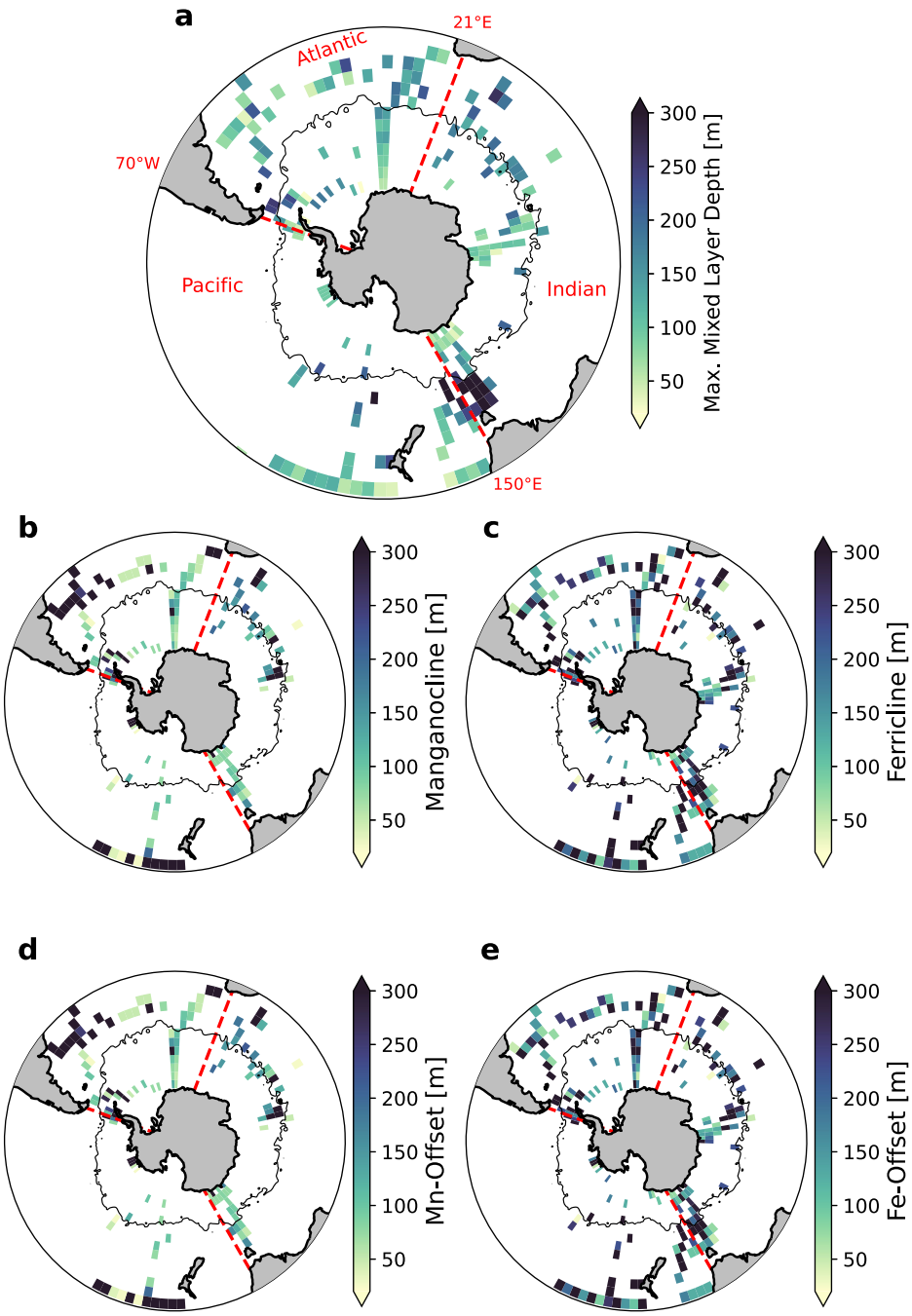

Fig. 1 | Spatial comparison of the maximum mixed layer depths, nutriclines and their offsets. Maps of **a** the annual maximum mixed layer depth (MLDmax; m), **b** the manganocline depth (ZMn; m), **c** the ferricline depth (ZFe; m), **d** the offset between the MLDmax and ZMn and **e** the offset between the MLDmax and ZFe. Please see the "Methods" for the definition of ZMn and ZFe. The red dashed lines show the boundaries between the major ocean basins of the Southern Ocean. The climatological position of the Antarctic Polar Front is shown in black, determined from the criteria outlined in literature[74]. The calculations were conducted on a 1° grid but are displayed on a 3° grid for visual clarity. While most datasets are obtained from the IDP 2025 database, additional datasets not yet included in the IDP are the samples collected during the ANA08B research expedition to the Amundsen Sea in 2017–2018 austral summer.

anomaly (σ_θ, kg m^{-3}) was used to trace both the nutricline and the pycnocline, which separates the deeper, denser waters from the lighter, upper waters. South of the polar front, denser waters dominate the upper ocean, and the $\sigma_\theta \geq 27$ kg m^{-3} isopycnal-associated with the subsurface maxima of Mn (ZMn) and Fe (ZFe) is present within these water masses. This indicates a region where a high supply of nutrients from subsurface to surface waters is expected (Supplementary Fig. 2). This potentially reflects stronger upwelling and vertical mixing south of the polar front, common in Southern Ocean frontal zones due to wind-driven Ekman divergence and reduced stratification.

Winter entrainment drives the supply of Fe and Mn

Differences in Mn and Fe entrainment stocks reflect metal-specific removal processes, particularly scavenging. For Mn, concentrations decrease with depth, meaning surface entrainment is largely controlled by the depth of the winter mixed layer and not by subsurface reservoirs below the nutricline. In contrast, Fe concentrations can remain elevated at depth, so entrainment may still draw on deeper subsurface stocks (Fig. 2). To assess the relative contributions of different physical processes, we find that winter entrainment is the dominant mechanism replenishing dMn (19 ± 5 μmol m^{-2} yr^{-1}; with mean ± standard deviation throughout the manuscript) to the mixed layer, contributing between 64 and 121% to the total physically driven supply across the Southern Ocean (Fig. 3a). Regional differences in winter entrainment stocks across basins likely reflect variations in winds and air-sea buoyancy fluxes, which control MLD and thus the size of the entrained reservoir. Mn winter entrainment was highest on average in the Indian basin (19 ± 4 μmol m^{-2} yr^{-1}), though values were comparable across basins within uncertainty (Supplementary Table 2). Similarly, winter entrainment dominated the physical supply of dFe (30 ± 5 μmol m^{-2} yr^{-1}), contributing 71–106% to the total dFe vertical supply (Fig. 3b). This is consistent with

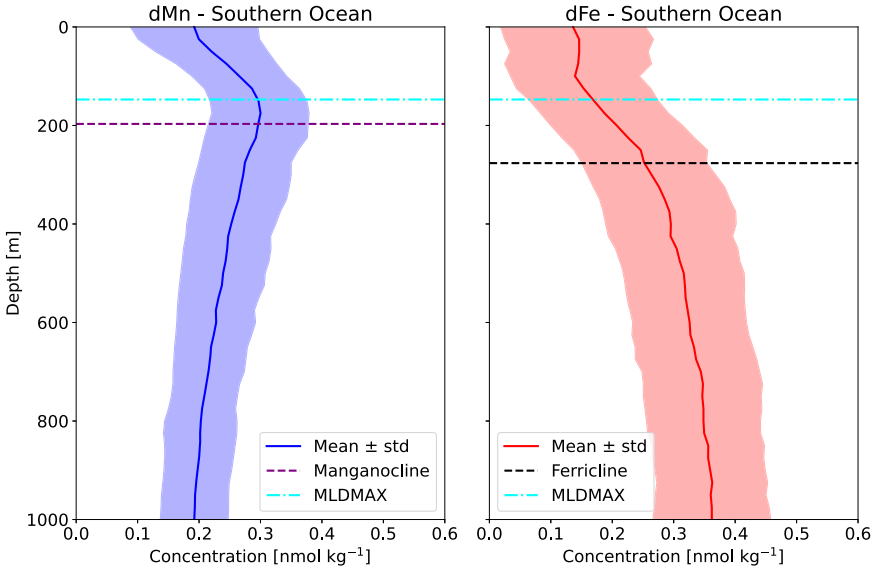

Fig. 2 | Vertical profiles of mean dissolved manganese (dMn) and dissolved iron (dFe) concentrations in the Southern Ocean. Solid lines show the mean profiles, and shaded areas indicate one standard deviation. Depth (m) is shown on the y-axis and concentration (nmol kg^{-1}) on the x-axis. The maximum mixed layer depth (MLDmax) and the mean manganocline and ferricline depths are indicated.

previous studies[35] that reported a mean Fe winter entrainment flux of 21 μmol m^{-2} yr^{-1} and a contribution of over 60% to the total vertical flux across the Southern Ocean. Mean Fe winter entrainment ranged from 32 to 36 ± 4–5 μmol m^{-2} yr^{-1} across the Southern Ocean basins, with values that were comparable within uncertainty (Supplementary Table 3). Comparable ZFe ranges indicate a similar vertical position of the Fe gradient and therefore similar entrainment of dFe into the mixed layer via deep winter mixing. Mean Fe entrainment exceeded Mn throughout the Southern Ocean, consistent with a larger subsurface (>200 m) Fe reservoir relative to Mn (Supplementary Fig. 3). Moreover, Fe winter entrainment was higher than Mn both north of the polar front (Fe: 33 ± 10 μmol m^{-2} yr^{-1}; Mn: 21 ± 5 μmol m^{-2} yr^{-1}) and south of the polar front (Fe: 27 ± 4 μmol m^{-2} yr^{-1}; Mn: 17 ± 4 μmol m^{-2} yr^{-1}). Differences in vertical entrainment stocks are reflected in water column distributions across the Southern Ocean basins. Low deep-water Mn concentrations relative to Fe may lead to Mn dilution (decreasing the Mn reservoir size) and Fe enrichment in the mixed layer, resulting in higher entrainment of Fe relative to Mn (Supplementary Fig. 3). The mean diapycnal diffusion flux of dMn across the Southern Ocean was 2 ± 1 μmol m^{-2} yr^{-1}, contributing 9–21% of the total dMn flux (Fig. 3c). Although these fluxes are generally positive, the direction of diffusive exchange can vary seasonally. During winter, when the mixed layer deepens below the subsurface dMn maximum (~100–150 m), vertical gradients weaken or reverse, leading to negative (downward) diffusive fluxes, while in spring and summer, shoaling of the mixed layer above the concentration maximum produces upward fluxes. The highest mean fluxes occurred in the Atlantic sector, which also showed the largest variability (0.8 ± 2.3 μmol m^{-2} yr^{-1}), followed by the Indian (0.5 ± 1.4) and Pacific (0.4 ± 0.6 μmol m^{-2} yr^{-1}) sectors. The mean dFe diffusive flux was slightly lower (0.6 ± 1.6 μmol m^{-2} yr^{-1}), contributing 2–20% of the total flux (Fig. 3d). Differences from previous estimates[35] (2.1 μmol m^{-2} yr^{-1}) likely arise from updated mixed-layer climatology and improved seasonal data coverage, refining vertical gradient estimates across basins.

Mean Ekman-driven Mn fluxes were 2 ± 15 μmol m^{-2} yr^{-1} across the Southern Ocean (Fig. 3e), with both net additions associated with Ekman upwelling and net losses associated with Ekman downwelling observed regionally. Net Mn additions ranged from 2 ± 18 to 3 ± 13 μmol m^{-2} yr^{-1}, while net losses reached −0.1 ± 14.1 μmol m^{-2} yr^{-1}. Similarly, mean Ekman-driven Fe fluxes were 4 ± 20 μmol m^{-2} yr^{-1} across the Southern Ocean (Fig. 3f), with net additions for Fe observed throughout the region. These additions ranged from 0.3 ± 20.5 to 1.4 ± 18.8 μmol m^{-2} yr^{-1}, with comparable magnitudes within uncertainty. For both Fe and Mn, there is a transition from Ekman convergence (downwelling) north of the polar front to Ekman divergence (upwelling) south of the polar front. This shift occurs as wind stress curl increases and changes sign from negative to positive south of the atmospheric subtropical jet, around 40°S[49,50].

The observed positive vertical fluxes of dFe and dMn reflect the combined influence of winter entrainment, diapycnal diffusion, Ekman upwelling, and remineralization, which together link subsurface and deep-water reservoirs to the surface mixed layer at the basin scale. Superimposed on these large-scale patterns, regional processes can locally enhance upward trace-metal transport. For example, around the Antarctic Peninsula, elevated sediment and porewater resuspension provide an additional subsurface source of dFe and dMn that can be upwelled or entrained into the mixed layer over time[51]. Fluxes may also be modulated by the vertical redistribution of atmospherically supplied trace metals, which can remain confined to the surface on timescales of days to weeks and stabilized by organic ligands[52]. In addition, interactions between currents and subsurface continental shelf topography can generate turbulent mixing events that promote the upward transport of dissolved trace metals across the mixed-layer depth[53].

While atmospheric deposition can contribute to total fluxes and, for Fe, supports a portion of Southern Ocean productivity[54], many inputs are highly localized near dust sources. As a result, dust-derived dFe and dMn inputs have a limited impact in much of the offshore Southern Ocean. We provide estimated atmospheric fluxes of Mn and Fe across different Southern Ocean basins[55–57] (Supplementary Table 4). Overall, trace-metal supply in the open ocean is dominated by vertical fluxes from entrainment, mixing, and remineralization, with Mn cycling primarily controlled by these internal ocean processes rather than external dust inputs[58].

Supply ratios drive phytoplankton co-limitation

Spatial and temporal variations in Mn:Fe supply ratios can decouple the net supply of these trace metals, influencing whether the biological requirements for one element over the other are met. Across the Southern Ocean, total physical Fe supply (Fig. 4a) exceeds that of Mn (Fig. 4b), with mean Fe:Mn supply ratios of 2 ± 1 north of the polar front and 1 ± 1 south of it (Fig. 4c). To better understand the biological implications of this supply imbalance, we applied the Mn limitation tracer (Mn*) alongside Fe:Mn supply ratios to diagnose potential regions of Fe, Mn, or co-limitation.

The Mn limitation tracer, averaged over the surface to 100 m, was previously defined as Mn* = dMn−(dFe/rFe:Mn)[1], where rFe:Mn represents the average Fe:Mn ratio of phytoplankton (an average value of 3.3, calculated from the 2.5[10] ratio for diatom dominated waters south of the polar front and 4.0[10] for haptophytes (flagellates) dominated waters north of the polar front[59]). Here we focus on stations within Southern Ocean high-

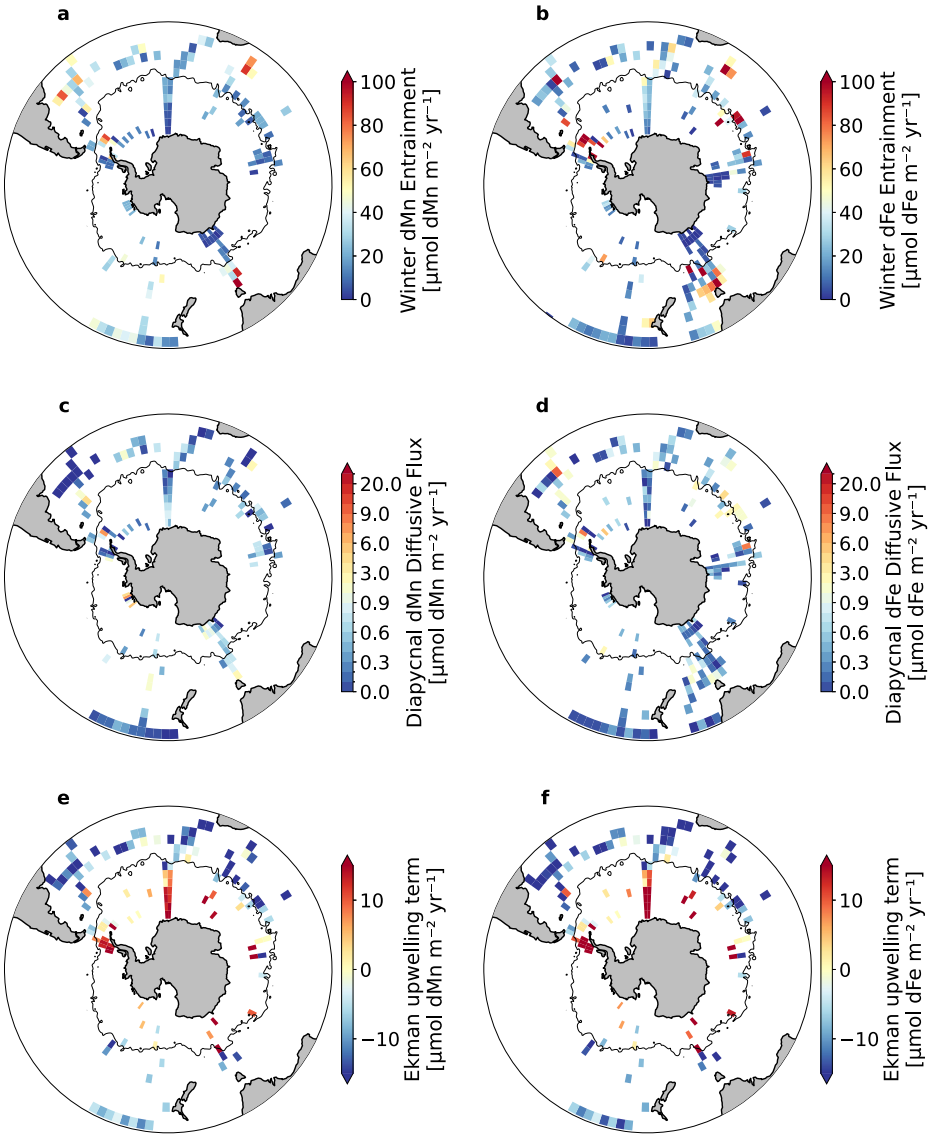

Fig. 3 | Physically-mediated processes driving the fluxes of dissolved Mn and dissolved Fe in the Southern Ocean. Maps of annual winter entrainment fluxes of **a** Mn and **b** Fe; annual diffusive fluxes of **c** Mn and **d** Fe; Ekman downwelling/upwelling fluxes of **e** Mn and **f** Fe. All fluxes are in units of μmol m^{-2} yr^{-1}. The climatological position of the Antarctic Polar Front is shown in black, determined from the criteria outlined in literature[74]. The calculations were conducted on a 1° grid but are displayed on a 3° grid for visual clarity. The data used here were collected as described in Fig. 1.

nutrient, low-chlorophyll (HNLC) waters to avoid including macronutrient-limited subtropical gyres, where Fe or Mn limitation is unlikely and could bias the interpretation of Mn* (Supplementary Fig. 4). Surface phosphate concentrations in the Southern Ocean typically average ~1.6 ± 0.2 μM south of 50°S and ~1.1 ± 0.4 μM north of 50°S[60]; therefore, stations with phosphate concentrations above ~1 μM were considered representative of macronutrient-replete HNLC waters. Although we apply fixed Fe:Mn ratios (2.5 and 4.0) based on diatom versus flagellate dominance, we acknowledge this is a simplification and that in reality there may be much more variability in this stoichiometry (Supplementary Fig. 5). Previous experimental work in the Drake Passage[6,61] has demonstrated robust Fe–Mn co-limitation in both diatoms[62] and picoeukaryotes, where they also assumed average cellular Fe:Mn ratios of approximately 2.7 to represent co-limited conditions. In our study, Mn* was positive and elevated (>0.15 nmol kg^{-1}) across the Southern Ocean, showing primary Fe limitation. Lower Mn* values (−0.10 to 0.08 nmol kg^{-1}) point to the potential for Fe–Mn colimitation or secondary Mn limitation regions, particularly in the central Drake Passage and along the zero meridian (Fig. 4d). This aligns with recent observations in the central Drake Passage, which showed that maximum photosynthetic efficiency was achieved only when Fe and Mn were supplied together during incubation experiments[6,61]. Our results also suggest potential Fe–Mn co-limitation along the polar front in the Indian sector (Fig. 4d). This aligns with previous modeling results[17] indicating high Mn limitation strength in the region; however, bioassay experiments are required to verify the occurrence of Mn limitation or Fe–Mn co-limitation.

Across the Southern Ocean basins, patterns in Mn* and Fe:Mn supply ratios show strong regional trends (Fig. 4c, d, and Supplementary Table 6). The Atlantic sector shows a variable Mn*, reaching down to ~0 nmol kg^{-1} in the central Drake passage (Atlantic mean 0.4 ± 0.4 nmol kg^{-1}), accompanied by a moderate physical supply Fe:Mn ratio (1.5 ± 0.9), indicating potential Mn–Fe limitation. In the Indian sector, Mn* averaged moderate values (0.18 ± 0.15 nmol kg^{-1}), and the high Fe:Mn supply ratio (1.18 ± 1.15) hints at potential Fe–Mn co-limitation. The Pacific had the highest Mn* values (0.7 ± 0.4 nmol kg^{-1}), indicative of Fe limitation, but Fe:Mn ratios were similar across basins (Pacific: 1.5 ± 0.6; Atlantic: 1.5 ± 0.6), indicating that potential Mn limitation is comparable between regions within the uncertainties. This decoupling between Mn* and Fe:Mn ratio may reflect more efficient Mn recycling relative to Fe removal in the Pacific sector. However, limited data coverage in the Pacific may also contribute to variability in Mn* and Fe:Mn ratio signals. In the Southern Ocean, Mn* values were comparable north (0.5 ± 0.4 nmol kg^{-1}) and south (0.5 ± 0.4 nmol kg^{-1}) of the polar front, although the Fe:Mn supply ratio was relatively higher to the north (1.6 ± 0.9) than to the south (1.3 ± 0.8). Overall, coupling (low Mn*,

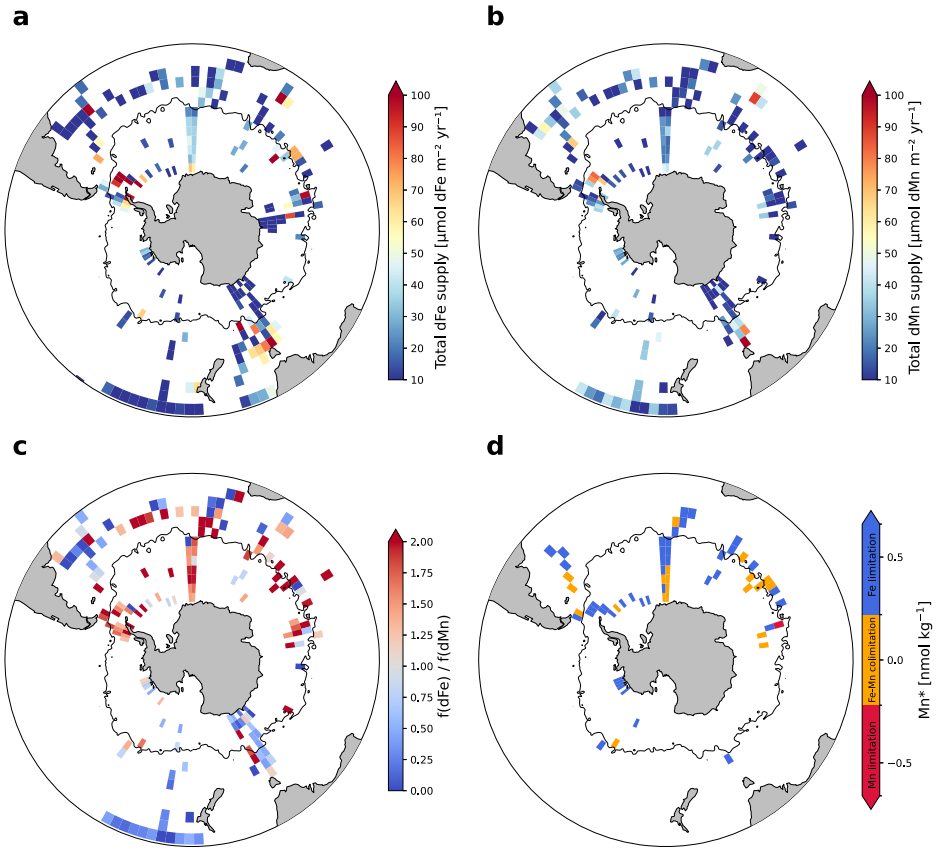

Fig. 4 | The relationship between the total internal physical supply of dissolved manganese and dissolved iron in the Southern Ocean. Maps of **a** total annual dFe supply (fdFe; µmol m^{-2} yr^{-1}), **b** total annual dMn supply (fdMn; µmol m^{-2} yr^{-1}), **c** Fe:Mn supply ratio, calculated as fdFe/fdMn, and **d** manganese co-limitation tracer (Mn*) showing Mn deficiency and potential Fe–Mn co-limitation in the surface Southern Ocean (0–100 m), calculated using Fe:Mn ratios of 2.510 south and 4.010 north of the polar front. Orange points indicate locations approaching Mn–Fe co-deficiency, and blue points represent sites with evidence of primary Fe limitation. Here, only high nutrients, low chlorophyll stations with elevated surface PO_4 concentrations are shown to avoid inclusion of macronutrient-limited subtropical waters. The climatological position of the Antarctic Polar Front is shown in black, determined from the criteria outlined in literature[74]. The calculations were conducted on a 1° grid but are displayed on a 3° grid for visual clarity. The data used here were collected as described in Fig. 1.

high Fe:Mn) is strongest in the Atlantic basin, suggesting potential Mn–Fe colimitation, while high Mn*, low Fe:Mn ratios in the Indian and Pacific sectors suggest more prevalent Fe limitation. The large standard deviations reflect notable spatial differences in Mn within each basin, indicating that averaging over entire basins at lower resolution may underestimate important local variations in Mn and Fe limitation. The use of a fixed Fe:Mn uptake ratio also introduces uncertainty, as it does not capture the natural variability in phytoplankton community structure and their physiological responses to trace metal availability.

Biogeochemical implications in a changing climate

Given the Southern Ocean's central role in the global carbon cycle[63], the regional decoupling between Fe and Mn supply and phytoplankton biological demand has important implications for primary production and ecosystem services[64]. Our findings highlight the importance of considering the physically—mediated supply of both Fe and Mn to understand phytoplankton productivity in the Southern Ocean, particularly given the large spatial differences in the supply mechanisms. The drivers of the upper-ocean physical processes (changes in buoyancy, oceanic currents and mixing) are already showing evidence of climate-driven changes. For example, pycnocline stratification has increased over recent decades, making vertical mixing weaker[65], especially in the Atlantic basin[66]. However, stronger surface turbulence from increases in wind stress has helped to deepen the mixed layer[65]. This turbulence can overcome stratification, resulting in upwelling-favorable conditions, allowing micronutrients like Mn and Fe to mix into the surface ocean. In summer, strong stratification can still reduce mixing efficiency despite these deeper mixed layers, thus slowing the rate of diapycnal diffusion and Ekman pumping. However, in winter, if turbulence keeps increasing, it could improve mixing and the recharge of surface nutrients through winter entrainment, depending on how strong and persistent the winds are. These changes in MLD not only influence the physical supply of Fe and Mn from below but also alter phytoplankton demands by modulating light availability, as shallower layers increase light exposure, which can stimulate growth and increase trace metal demand[67,68]. Altogether, these physical and biological processes dictate the seasonal availability of Fe and Mn. By decoupling the physical fluxes of Fe and Mn, we can identify localized regions of potential Mn–Fe co-limitation and providing a process-based, spatially resolved understanding of trace metal dynamics in the Southern Ocean.

Methods

Database data collection

The dissolved trace metal and phosphate (PO_4) data used in this study, including both concentration and hydrography south of 30°S, were downloaded from the *GEOTRACES IDP* 2025 database[47]. Additional datasets used in this study, not yet included in the IDP, are samples collected during the ANA08B research expedition to the Amundsen Sea in 2017–2018 austral summer (see Supplementary Fig. 6 for a plot of all sample locations used in this study). All samples were collected and analysed following standard GEOTRACES protocols, consistent with methods used on previously published GEOTRACES cruises. The Argo float data[69], collected and made freely available by the International Argo Program and contributing national programs (https://argo.ucsd.edu, https://www.ocean-ops.org), are part of the Global Ocean Observing System.

Data processing and interpolation

The combined database was processed similarly to previous methods[35] with modifications as follows. The data was regridded into 1° × 1° longitude and latitude bins, interpolated on a uniform depth grid with a 25 m depth resolution in the upper 1000 m, as it comprises the maximum mixing over the year across the Southern Ocean. Different depth conditions were applied to the interpolated data: we first conditioned the data to have at least one observation in the upper 50 m, at least one observation deeper than 400 m and finally at least five observations per station. A Pchip interpolation

method was then applied to the resulting profiles to interpolate variables (Mn and Fe concentrations and potential density) within the depth range bins. The concentration at the depth of 0 m was taken as the concentration at the first depth of 25 m.

Data validation

Before using the interpolated data, we performed a control check to assess the validity and reproducibility of the regridding and PCHIP interpolation approach. Validation was carried out by reproducing previously published results from the well-resolved SCALE 2019 dataset[36] and the SR3 transect (Supplementary Figs. 7 and 8). To minimize sensitivity to data resolution, interpolation was only applied to stations meeting strict conditioning criteria: at least one observation in the upper 50 m, one deeper than 400 m, and a minimum of five depth levels per station. Under these conditions, seasonal MLDs reproduced the published results with mean differences of 3.10 m in winter and 9.24 m in spring, while total dMn fluxes differed by only 0.15 μmol m^{-2} yr^{-1}, indicating robust performance of the interpolation.

Vertical flux calculations of dMn and Fe

The dMn and dFe gradients with depth (∂dMn/∂z and ∂dFe/∂z) were computed using the nearest neighbor method. ZMn and ZFe were calculated as the depth (<1000 m) where ∂dMn/∂z and ∂dFe/∂z are maximal. Winter entrainment was estimated by integrating dMn and dFe from the surface (0 meters) down to the maximum mixed layer (MLDmax) depth at each station, obtained from the Argo database. The winter-entrained dMn and dFe stock that is detrained during spring mixed layer shallowing was estimated as the ratio between MLDmin and MLDmax multiplied by the winter entrainment flux. Diapycnal diffusion was calculated by taking ∂dFe/∂z and ∂dMn/∂z at the MLD and multiplying by an estimate of the vertical diffusivity (k_z). We used an average K_z of 10^{-4} m^2 s^{-1}, representing the geometric mean of commonly reported open-ocean values (10^{-5}–10^{-3} m^2 s^{-1})[70]. Ekman pumping, which represents the vertical movement of water driven by westerly winds, Coriolis force from Earth's rotation, and inertial forces[71], was calculated by multiplying the surface northwards and eastwards component of the wind stress curl (kg m^{-1} s^{-2}) with the mean mixed layer dFe and dMn concentrations (nmol kg^{-1}), the Coriolis force (s^{-1}) and density (kg m^{-3}). The wind stress components were obtained from the Copernicus Climate Change Service (C3S) ERA5, which is the fifth generation of the European Center for Medium-Range Weather Forecasts atmospheric reanalysis of the global climate (Copernicus Climate Change Service, 2017). Negative Ekman fluxes indicate downwelling, while positive values represent upwelling.

Mixed layer and nutricline depths estimation

The MLD was calculated using CTD sensor data and co-located ARGO float profiles where they are available, using a density threshold method[72], defined as the depth where the interpolated potential density exceeds the surface density (10 m) by more than 0.03 kg m^{-3}. Co-locating the CTD and ARGO profiles involved applying a weighting factor of ($1/d^4$) for the same month and year of sampling, where d represents the distance between the in situ CTD measurements and the ARGO profiles. The average weighting factor within the study region was 1.36×10^{-4} (Supplementary Fig. 9), suggesting that the distances between CTD and ARGO profiles were relatively small. Similarly, applying this factor had little to no effect on the MLD values, suggesting that the MLD was relatively insensitive to the small distances between the CTD and ARGO profiles.

To determine ZFe and ZMn, the processed profiles were vertically interpolated, identifying the depths (<1000 m) at which the vertical gradients (∂dFe/∂z and ∂dMn/∂z) were greatest. To avoid bias from sediment-driven signals in coastal systems, profiles where ZFe occurred at more than 80% of the bottom depth were excluded.

Data availability

All data used in this study are publicly available in the IDP2025. Data from the Amundsen Sea is available at https://doi.org/10.25850/nioz/7b.b.bd.

Code availability

The Python script used in this study is made available on GitHub at https://github.com/Thapelo934/Physical-vertical-fluxes.git.

Received: 10 November 2025; Accepted: 19 March 2026;
Published online: 18 May 2026

References

1. Raven, J. A. Predictions of Mn and Fe use efficiencies of phototrophic growth as a function of light availability for growth and of C assimilation pathway. *New Phytol.* **116**, 1–18 (1990).
2. Twining, B. S. & Baines, S. B. The trace metal composition of marine phytoplankton. *Ann. Rev. Mar. Sci.* **5**, 191–215 (2013).
3. Boyd, P. W. et al. Multi-faceted particle pumps drive carbon sequestration in the ocean. *Nature* **568**, 327–335 (2019).
4. Wedepohl, K. H. The composition of the continental crust. *Geochim. Cosmochim. Acta* **59**, 1217–1232 (1995).
5. Moore, C. et al. Processes and patterns of oceanic nutrient limitation. *Nat. Geosci.* **6**, 701–710 (2013).
6. Browning, T. J. et al. Manganese co-limitation of phytoplankton growth and major nutrient drawdown in the Southern Ocean. *Nat. Commun.* **12**, 884 (2021).
7. Latour, P., Strzepek, R. F., Wuttig, K., Van Der Merwe, P. & Eggins, S. Seasonality of phytoplankton growth limitation by iron and manganese in subantarctic waters. *Elem. Sci. Anthr.* **11**, 00022 (2023).
8. Strzepek Robert, F., Maldonado Maria, T., Hunter Keith, A., Frew Russell, D. & Boyd Philip, W. Adaptive strategies by Southern Ocean phytoplankton to lessen iron limitation: uptake of organically complexed iron and reduced cellular iron requirements. *Limnol. Oceanogr.* **56**, https://doi.org/10.4319/lo.2011.56.6.1983 (2011).
9. Strzepek, R. F., Boyd, P. W. & Sunda, W. G. Photosynthetic adaptation to low iron, light, and temperature in Southern Ocean phytoplankton. *Proc. Natl. Acad. Sci. USA* **116**, 4388–4393 (2019).
10. Merchant, S. S. & Helmann, J. D. Elemental economy: microbial strategies for optimizing growth in the face of nutrient limitation. *Adv. Microb. Physiol.* **60**, 1–210 (2012).
11. Valenti, R., Jabłońska, J. & Tawfik, D. S. Characterization of ancestral Fe/Mn superoxide dismutases indicates their cambialistic origin. *Protein Sci.* **31**, 1–14 (2022).
12. Frye, K. A., Sendra, K. M., Waldron, K. J. & Kehl-Fie, T. E. Old dogs, new tricks: new insights into the iron/manganese superoxide dismutase family. *J. Inorg. Biochem.* **230**, 111748 (2022).
13. Tabares, L. C., Bittel, C., Carrillo, N., Bortolotti, A. & Cortez, N. The single superoxide dismutase of Rhodobacter capsulatus is a cambialistic, manganese-containing enzyme. *J. Bacteriol.* **185**, 3223–3227 (2003).
14. Anugerahanti, P. & Tagliabue, A. Process controlling iron-manganese regulation of the Southern Ocean biological carbon pump. *Philos. Trans. A Math. Phys. Eng. Sci.* **381**, 20220065 (2023).
15. Sunda, W. G. & Huntsman, S. A. Effect of Zn, Mn, and Fe on Cd accumulation in phytoplankton: Implications for oceanic Cd cycling. *Limnol. Oceanogr.* **45**, 1501–1516 (2000).
16. Irving, H. & Williams, R. J. P. 637. The stability of transition-metal complexes. *J. Chem. Soc*. 3192–3210, https://doi.org/10.1039/JR9530003192 (1953).
17. Hawco, N. J., Tagliabue, A. & Twining, B. S. Manganese limitation of phytoplankton physiology and productivity in the Southern Ocean. 1–39 https://doi.org/10.1029/2022GB007382 (2022).
18. Lewis, B. L. & Luther III, G. W. Processes controlling the distribution and cycling of manganese in the oxygen minimum zone of the Arabian Sea. *Deep Sea Res. Part II Top. Stud. Oceanogr.* **47**, 1541–1561 (2000).
19. Sunda, W. G. & Huntsman, S. A. Photoreduction of manganese oxides in seawater. *Mar. Chem.* **46**, 133–152 (1994).

20. Dick, G. J. et al. Enzymatic microbial Mn(II) oxidation and Mn biooxide production in the Guaymas Basin deep-sea hydrothermal plume. *Geochim. Cosmochim. Acta* **73**, 6517–6530 (2009).
21. Middag, R. D., De Baar, H. J. W., Laan, P., Cai, P. V. & Van Ooijen, J. C. Dissolved manganese in the Atlantic sector of the Southern Ocean. *Deep Sea Res. Part II Top. Stud. Oceanogr.* **58**, 2661–2677 (2011).
22. Klinkhammer, G. P. & Bender, M. L. The distribution of manganese in the Pacific Ocean. *Earth Planet. Sci. Lett.* **46**, 361–384 (1980).
23. Cheize, M. et al. Contribution of resuspended sedimentary particles to dissolved iron and manganese in the ocean: an experimental study. *Chem. Geol.* **511**, 389–415 (2019).
24. Middag, R., de Baar, H. J. W., Klunder, M. B. & Laan, P. Fluxes of dissolved aluminum and manganese to the Weddell Sea and indications for manganese co-limitation. *Limnol. Oceanogr.* **58**, 287–300 (2013).
25. Van Hulten, M. et al. Manganese in the west Atlantic Ocean in the context of the first global ocean circulation model of manganese. *Biogeosciences* **14**, 1123–1152 (2017).
26. Rijkenberg, M. J. et al. The distribution of dissolved iron in the West Atlantic Ocean. *PloS ONE* **9**, e101323 (2014).
27. Chen, X. G. et al. Controls on distributions of aluminium, manganese and cobalt in the South Atlantic Ocean along GEOTRACES transect GA10. *Geochim. Cosmochim. Acta* **373**, 177–196 (2024).
28. Berger, C. J. M., Lippiatt, S. M., Lawrence, M. G. & Bruland, K. W. Application of a chemical leach technique for estimating labile particulate aluminum, iron, and manganese in the Columbia River plume and coastal waters off Oregon and Washington. *J. Geophys. Res.* **113**, C00B01 (2008).
29. Westerlund, S. & Öhman, P. Iron in the water column of the Weddell Sea. *Mar. Chem.* **35**, 199–217 (1991).
30. Klunder, M. B., Laan, P., Middag, R., De Baar, H. J. W. & van Ooijen, J. C. Dissolved iron in the Southern Ocean (Atlantic sector). *Deep Sea Res. Part II Top. Stud. Oceanogr.* **58**, 2678–2694 (2011).
31. Parekh, P., Follows, M. J. & Boyle, E. A. Decoupling of iron and phosphate in the global ocean. *Glob. Biogeochem. Cycles* **19**, 1–16 (2005).
32. Oldham, V. E. *The Complexation Chemistry of Dissolved Manganese(III) in the Ocean and its Role in the Coupled Cycles of Carbon, Iron and Sulfur*. PhD thesis, Univ. Delaware (2017).
33. Van Horsten, N. *Insights into Early Winter Southern Indian Ocean Dissolved Iron Distributions and Remineralisation using Excess Barium (GEOTRACES GIPr07 cruise)*. PhD thesis, Stellenbosch Univ. (2022).
34. Mikaloff Fletcher, S. E. et al. Inverse estimates of anthropogenic CO_2 uptake, transport, and storage by the ocean. *Glob. Biogeochem. Cycles* **20**, https://doi.org/10.1029/2005GB002530 (2006).
35. Tagliabue, A. et al. Surface-water iron supplies in the Southern Ocean sustained by deep winter mixing. *Nat. Geosci.* **7**, 314–320 (2014).
36. Ramalepe, T., Samanta, S., Cloete, R., Ryan-Keogh, T. J. & Roychoudhury, A. N. Winter entrainment drives the mixed layer supply of manganese in the Southern Ocean. **1**, 1–12, https://doi.org/10.1002/lno.12634 (2024).
37. Painter, S. C. et al. An assessment of the vertical diffusive flux of iron and other nutrients to the surface waters of the subpolar north Atlantic Ocean. *Biogeosciences* **11**, 2113–2130 (2014).
38. Oschlies, A. Nutrient supply to the surface waters of the North Atlantic: a model study. *J. Geophys. Res. Ocean* **107**, https://doi.org/10.1029/2001JC000888 (2002).
39. Nicholson, S., Lévy, M., Llort, J., Swart, S. & Monteiro, P. M. S. Investigation into the impact of storms on sustaining summer primary productivity in the sub-Antarctic Ocean. *Geophys. Res. Lett.* **43**, 9192–9199 (2016).
40. Sunda, W. G. & Huntsman, S. A. Effect of sunlight on redox cycles of manganese in the southwestern Sargasso Sea. *Deep Sea Res. Part A Oceanogr. Res. Pap.* **35**, 1297–1317 (1988).
41. Rijkenberg, M. J. A. et al. The influence of UV irradiation on the photoreduction of iron in the Southern Ocean. *Mar. Chem.* **93**, 119–129 (2005).
42. Janssen, D. J. et al. Trace metal and nutrient dynamics across broad biogeochemical gradients in the Indian and Pacific sectors of the Southern Ocean. *Mar. Chem.* **221**, 103773 (2020).
43. Frew, R. D. et al. Particulate iron dynamics during FeCycle in subantarctic waters southeast of New Zealand. *Glob. Biogeochem. Cycles* **20**, https://doi.org/10.1029/2005GB002558 (2006).
44. Croot, P. L. et al. Physical mixing effects on iron biogeochemical cycling: FeCycle experiment. *J. Geophys. Res. Oceans* **112**, https://doi.org/10.1029/2006JC003748, (2007).
45. Rigby, S. J., Williams, R. G., Achterberg, E. P. & Tagliabue, A. Resource availability and entrainment are driven by offsets between nutriclines and winter mixed-layer depth. *Glob. Biogeochem. Cycles* **34**, 1–18 (2020).
46. Ryan-Keogh, T. J., Thomalla, S. J., Monteiro, P. M. & Tagliabue, A. Multidecadal trend of increasing iron stress in Southern Ocean phytoplankton. *Science* **379**, 834–840 (2023).
47. GEOTRACES Intermediate Data Product Group (2025). The GEOTRACES Intermediate Data Product 2025 (IDP2025). NERC EDS British Oceanographic Data Centre NOC, https://doi.org/10.5285/42c92148-8d03-8be6-e063-7086abc09f0c.
48. Blain, S., Sarthou, G. & Laan, P. Distribution of dissolved iron during the natural iron-fertilization experiment KEOPS (Kerguelen Plateau, Southern Ocean). *Deep Sea Res. Part II Top. Stud. Oceanogr.* **55**, 594–605 (2008).
49. Gille, S. T., Carranza, M. M., Cambra, R. & Morrow, R. Wind-induced upwelling in the Kerguelen Plateau region. *Biogeosciences* **11**, 6389–6400 (2014).
50. McPhaden, M. J., Cronin, M. F. & McClurg, D. C. Meridional structure of the seasonally varying mixed layer temperature balance in the eastern tropical Pacific. *J. Clim.* **21**, 3240–3260 (2008).
51. Middag, R., De Baar, H. J. W., Laan, P. & Huhn, O. The effects of continental margins and water mass circulation on the distribution of dissolved aluminum and manganese in Drake Passage. *J. Geophys. Res. Ocean.* **117**, C05045 (2012).
52. Bressac, M. et al. Subsurface iron accumulation and rapid aluminum removal in the mediterranean following African dust deposition. *Biogeosciences* **18**, 6435–6453 (2021).
53. Katsumata, K., Talley, L. D., Capuano, T. A. & Whalen, C. B. Spatial and temporal variability of diapycnal mixing in the Indian Ocean. *J. Geophys. Res. Ocean* **126**, e2021JC017728 (2021).
54. Weis, J. et al. One-third of Southern Ocean productivity is supported by dust deposition. *Nature* **629**, 603–608 (2024).
55. Mahowald, N. M. et al. Atmospheric global dust cycle and iron inputs to the ocean. *Glob. Biogeochem. Cycles* **19**, GB4025 (2005).
56. Chance, R., Jickells, T. D. & Baker, A. R. Atmospheric trace metal concentrations, solubility and deposition fluxes in remote marine air over the southeast Atlantic. *Mar. Chem.* **177**, 45–56 (2015).
57. Rudnick, R. L. & Gao, S. Composition of the continental crust. *Treatise Geochem.* **3**, 1–64 (2003).
58. Baker, A. R. et al. Trace element and isotope deposition across the air–sea interface: progress and research needs. *Philos. Trans. R. Soc. A Math. Phys. Eng. Sci.* **374**, 20160106 (2016).
59. Hayward, A., Law, C. S., Pinkerton, M. H., Wright, S. W. & Gutiérrez-Rodriguez, A. Twenty-six years of phytoplankton pigments reveal a circumpolar class divide around the Southern Ocean. *Commun. Earth Environ.* **4**, 4–10 (2024).
60. Yoon, J. E. et al. Reviews and syntheses: ocean iron fertilization experiments–past, present, and future looking to a future Korean iron fertilization experiment in the Southern Ocean (KIFES) project. *Biogeosciences* **15**, 5847–5889 (2018).

61. Balaguer, J. et al. Iron and manganese co-limit the growth of two phytoplankton groups dominant at two locations of the Drake Passage. *Commun. Biol.* **5**, 207 (2022).
62. Pausch, F., Bischof, K. & Trimborn, S. Iron and manganese co-limit growth of the Southern Ocean diatom *Chaetoceros debilis*. *PLoS ONE* **14**, e0215824 (2019).
63. Gruber, N., Landschützer, P. & Lovenduski, N. S. The variable Southern Ocean carbon sink. *Annu. Rev. Mar. Sci.* **11**, 159–184 (2019).
64. Person, R. et al. Sensitivity of ocean biogeochemistry to the iron supply from the Antarctic ice sheet explored with a biogeochemical model. *Biogeosciences* **16**, 3583–3603 (2019).
65. Sallée, J. B. et al. Summertime increases in upper-ocean stratification and mixed-layer depth. *Nature* **591**, 592–598 (2021).
66. Buongiorno Nardelli, B. & Iudicone, D. A dynamical geography of observed trends in the global ocean. *Sci. Adv.* **11**, eaav3532 (2025).
67. Strzepek, R., Hunter, K., Frew, R., Harrison, P. & Boyd, P. Iron–light interactions differ in Southern Ocean phytoplankton. *Limnol. Oceanogr.* **57**, 1182–1200 (2012).
68. Sverdrup, H. U. On conditions for the vernal blooming of phytoplankton. *J. Cons. Int. Explor. Mer.* **18**, 287–295 (1953).
69. Wong, A. P. S. et al. Argo data 1999–2019: two million temperature-salinity profiles and subsurface velocity observations from a global array of profiling floats. *Front. Mar. Sci.* **7**, 258 (2020).
70. Cisewski, B., Strass, V. H. & Prandke, H. Upper-ocean vertical mixing in the Antarctic Polar Front zone. *Deep Sea Res. Part II Top. Stud. Oceanogr.* **52**, 1087–1108 (2005).
71. Morrison, A. K., Frölicher, T. L. & Sarmiento, J. L. Upwelling in the Southern Ocean. *Phys. Today* **68**, 27–32 (2015).
72. Monte, D. B., Madec, G., Fischer, A. S., Lazar, A. & Iudicone, D. Mixed layer depth over the global ocean: an examination of profile data and a profile-based climatology. *J. Clim.* **17**, 109–123 (2004).
73. Schlitzer, R. & Mieruch-Schnülle, S. webODV explore. Available at: https://explore.webodv.awi.de (2021).
74. Orsi, A. H., Whitworth, T. & Nowlin, W. D. On the meridional extent and fronts of the Antarctic circumpolar current. *Deep Sea Res. Part I Oceanogr. Res. Pap.* **42**, 641–673 (1995).

Acknowledgements

We thank all the scientists who contributed dissolved manganese and iron data through the GEOTRACES programme (www.geotraces.org). The GEOTRACES 2025 Intermediate Data Product (IDP2025) represents an international collaboration and is endorsed by the Scientific Committee on Oceanic Research (SCOR). The GEOTRACES data were explored and downloaded via an online data extraction service at https://geotraces.webodv.awi.de/[73]. Many researchers and funding agencies responsible for the collection of data and quality control are thanked for their contributions to the IDP2025. Many thanks to R. Middag and M. van Manen for providing pre-publication raw concentration data. We also appreciate the efforts of O. Valk, M. Sitofile, T. Mtshali, and M. Tsanwani in collecting and analyzing the Gough 2023 trace metal samples. Furthermore, we acknowledge S. Samanta and R. Cloete for their contributions to the collection and analysis of the 2017 winter data. We would also like to thank the South African National Antarctic Program (SANAP) and the captain and crew of the SA Agulhas II. This research was supported by funds to A.N.R. from an anonymous Donor Trust as part of the Whales and Climate Research Program (whalesandclimate.org). T.R., T.R.K. were supported through the CSIR's Southern Ocean Carbon-Climate Observatory funded by the Department of Science and Innovation (DSI/CON C3184/2023), the CSIR's Parliamentary Grant (0000005278) and the National Research Foundation South African National Antarctic Programme (SANAP200511521175; SANAP23042496681).

Author contributions

T.R. designed and conceptualized the study, calculated manganese, iron, and physical flux data, wrote the original draft, and performed data synthesis. A.N.R., T.J.R.-K. supervised the project, provided critical review, and revised the manuscript. C.B., E.B., N.v.H., H.P., Y.S. and L.Z. contributed to data analysis, processing, and interpretation. A.B., P.L. and G.S. contributed to the study design and interpretation of results. All authors discussed the results and implications and reviewed and revised the manuscript.

Competing interests

The authors declare no competing interests.

Additional information

Supplementary information The online version contains Supplementary material available at https://doi.org/10.1038/s43247-026-03466-3.

Correspondence and requests for materials should be addressed to Thapelo Ramalepe.

Peer review information *Communications Earth and Environment* thanks the anonymous reviewers for their contribution to the peer review of this work. Primary handling editors: José Luis Iriarte Machuca and Alice Drinkwater. A peer review file is available.